Journal of Materiomics 7 (2021) 721–727

Contents lists available at ScienceDirect

Journal of Materiomics

journal homepage: www.journals.elsevier.com/journal-of-materiomics/

# Fabrication of CDs hybrid MIL-68(In) derived $In_2O_3$–$In_2S_3$ hollow tubular heterojunction and their exceptional self-powered PEC aptasensing properties for ampicillin detecting

Tao Yan [a, *], Yixuan Feng [a], Xiang Ren [b], Jinkai Li [c], Yizhong Lu [c], Meng Sun [a], Liangguo Yan [a], Qin Wei [b], Huangxian Ju [b]

[a] School of Water Conservancy and Environment, University of Jinan, China Key Laboratory of Interfacial, Jinan, 250022, China
[b] Key Laboratory of Interfacial Reaction & Sensing Analysis in Universities of Shandong, School of Chemistry and Chemical Engineering, University of Jinan, Jinan, 250022, China
[c] School of Materials Science and Engineering, University of Jinan, Jinan, 250022, China

ARTICLE INFO

*Article history:*
Received 3 April 2020
Received in revised form
27 December 2020
Accepted 10 January 2021
Available online 16 January 2021

*Keywords:*
Self-powered
Photoelectrochemical aptasensor
MIL-68(In)-derived
Hollow tubes
Ampicillin

ABSTRACT

A visible-light-driven self-powered photoelectrochemical (PEC) aptasensor was developed for ampicillin (AMP) detecting based on carbon dots (CDs) hybrid MIL-68(In)-derived $In_2O_3$–$In_2S_3$ hollow tubular heterojunction (CDs/$In_2O_3$–$In_2S_3$). $In_2S_3$ nanosheets uniformly grew in-situ on the surface of $In_2O_3$ hollow tubes, forming a close contact heterogeneous interface, which significantly promoted the transfer and separation of photo-generated carriers, and provided a large specific surface area and rich active sites for the PEC aptasensing platform. Furthermore, the CDs/$In_2O_3$–$In_2S_3$/ITO electrode, which was obtained by dipping assembly, showed remarkable and stable photoelectric signals at zero-bias under visible light irradiation. The amino-functionalized AMP aptamer was fixed on the working electrode as a biological recognition element, and the concentration of AMP was determined by observing the change in photocurrent intensity caused by the specific capture of AMP molecules in solution. Under optimized conditions, the developed PEC aptasensor displayed a relatively wide linear range from 0.001 ng $mL^{-1}$ to 300 ng $mL^{-1}$, as well as a low detection limit (LOD) of 0.06 pg $mL^{-1}$. Besides, the novel self-powered PEC AMP-aptasensor exhibited excellent reproducibility, good stability and selectivity, which open a potential avenue for antibiotic residues detection in environmental media.



## 1. Introduction

Ampicillin (AMP), a commonly used $\beta$-lactam antibiotic, has been widely used in medicine and agriculture to treat various bacterial infections [1]. However, excessive use and residues of antibiotics in agriculture and animal husbandry can lead to serious food and environmental safety problems that endanger the health of human and animal [2,3]. In recent years, many approaches have been established for APM detection, including high performance liquid chromatography (HPLC) [4], Raman spectroscopy [5], fluorescence [6], electrochemical technique [7], and so on. However, these methods have more or less disadvantages such as large equipment, cumbersome operation, and high cost, which limit their applications to a certain extent. Hence, it is urgent to develop a rapid, efficient, and sensitive technology for AMP detecting.

In the past ten years, optoelectronic devices such as photovoltaic cell [8], thin film transistors [9], and diode [10], etc, have shown potential prospects in the field of photocatalysis. Among them, the photoelectrochemical (PEC) sensor based on photo-induced electron transfer at electrode/interface has become an emerging analytical technique and attracted widespread attention due to its high sensitivity, low background, convenient operation, and low cost [11,12]. Recently, self-powered PEC sensors has been developed rapidly, and the significant advantage is that its detecting can be operated by the photo-generated current without any external power supply [13–15]. Moreover, no extra voltage is input, the self-powered PEC sensors can eliminate the influence of oxidizing/reducing substances and weaken

* Corresponding author.
*E-mail addresses:* yantujn@163.com (T. Yan), 18253131392@163.com (Y. Feng), xiangren8901@gmail.com (X. Ren), mes_lijk@ujn.edu.cn (J. Li), mes_liyz@ujn.edu.cn (Y. Lu), smlcu@163.com (M. Sun), yanyu-33@163.com (L. Yan), sdjndxwq@163.com (Q. Wei), hxju@nju.edu.cn (H. Ju).
Peer review under responsibility of The Chinese Ceramic Society.

https://doi.org/10.1016/j.jmat.2021.01.002

the harm to biomolecules on the electrode surface, thus achieving sensitive detection [16]. Nevertheless, the poor selectivity of PEC sensing is still a key factor to achieve sensitive detection. Aptamer, as a biological building block with high recognition ability for target molecules, has been favorably employed to the detection of antibiotics [17], inorganic ions [18], cells [19], and various proteins [20]. Therefore, it is predicted that the outstanding specificity of well-designed aptamer combined with self-powered PEC sensing strategy is a promising analytical approach for the future.

For efficient PEC detection device, the core component is a well-designed photoactive matrix with brilliant photoelectric conversion properties. It is worth noting that the morphology and structure of nanomaterials have great influence on their properties, which make them showed unique properties in various fields [21–24]. Recently, various micro/nano structures derived from MOFs as a precursor or template have been extensively studied by scholars at home and abroad, which inherits the inherent advantages of original MOFs, including porous structure, a large specific surface, abundant active sites and adjustable structure [25]. Among various derivative, the unique hollow architectures are conducive to adjust the refractive index in the void of space to improve light utilization, and provide abundant exposed active sites for the specific catalytic reaction [26,27]. Besides, the hollow cavity is beneficial to shorten the charge transfer length from the inside to the surface, thus effectively promote the separation of photogenerated carrier [28]. Reviewing the studies regarding MOFs-derived hollow structures, Lou's group developed In-MOF-derived $In_2S_3/CdIn_2S_4$ [29] and $ZnIn_2S_4/In_2O_3$ [30] for $CO_2$ photoreduction, which provided a new idea for developing hollow tubular heterojunctions. Analogously, Zhang's group designed a novel $CdS/In_2O_3$ hierarchical nanotube heterostructure based on MIL-68(In) for photocatalytic hydrogen production [31]. Lu's group synthesized $In_2O_3$@$ZnFe_2O_4$ heterojunction by loading $ZnFe_2O_4$ nanosheets on the surface of $In_2O_3$ hollow tube derived from MIL-68(In), which exhibited good photocatalytic degradation performance [32]. Additionally, Carbon dots (CDs), as a promising zero-dimensional quantum dots, have been extensively employed in multifarious fields due to its unique electrical and optical properties [33–35]. Especially, the up-conversion PL performance and high conductivity of CDs are ideal for improving the photoelectric response of PEC sensor [36]. Therefore, it is more desirable to fabricate high-efficiently CDs-based materials for more promising PEC device.

In this work, a novel self-powered PEC aptasensing platform based on the $CDs/In_2O_3–In_2S_3$ composite for AMP detection was developed, as illustrated in Scheme 1. The $In_2O_3–In_2S_3$ hollow tubular heterojunction was successful constructed by the in-situ growth of oriented $In_2S_3$ nanosheets on surfaces of $In_2O_3$ hollow tubes through low temperature hydrothermal ion exchange process. And the CDs was adopted as a photosensitizer for signal amplification, which synthesized by simple hydrothermal method. The PEC performance of the as-prepared $CDs/In_2O_3–In_2S_3$ composite was investigated systematically. Due to the widened visible light absorption range and enhanced photoelectric conversion efficiency, the $CDs/In_2O_3–In_2S_3$/ITO electrode displayed excellent PEC performance at zero-bias under visible light irradiation. Moreover, the aptamer was modified on the working electrode as a specific recognition unit, which remarkably improved the selectivity of the aptasenser, achieving the rapid, accurate and sensitive analysis of AMP.

## 2. Experimental methods

### 2.1. Preparation of MIL-68(In) derived $In_2O_3–In_2S_3$ hollow tubular heterojunction

The $In_2O_3$ hollow tubes was synthesized by thermal annealing of hexagonal MIL-68(In) precursors. Firstly, the MIL-68(In) was prepared according to previous literature with some modifications [37]. Typically, $In(NO_3)_3·xH_2O$ (1.8 mmol) and 1, 4 - benzenedicarboxylic acid (1.8 mmol) were mixed in 15 mL of DMF, followed by adding 80 μL of 0.04 mol $L^{-1}$ NaOAc solution with continuous stirring. Then, the mixture was transferred in an oil bath and heated at 100 °C for 30 min. After cooling to room-temperature (25 °C), the precipitates were successively rinsed with distilled water and absolute ethanol for several times, and then dried in vacuum at 60 °C for 12 h. Finally, the obtained solid powder was placed into a quartz boat and annealed at 500 °C for 1 h in air with a heating rate of 2 °C·$min^{-1}$. Finally, the faint yellow $In_2O_3$ hollow tubes was obtained.

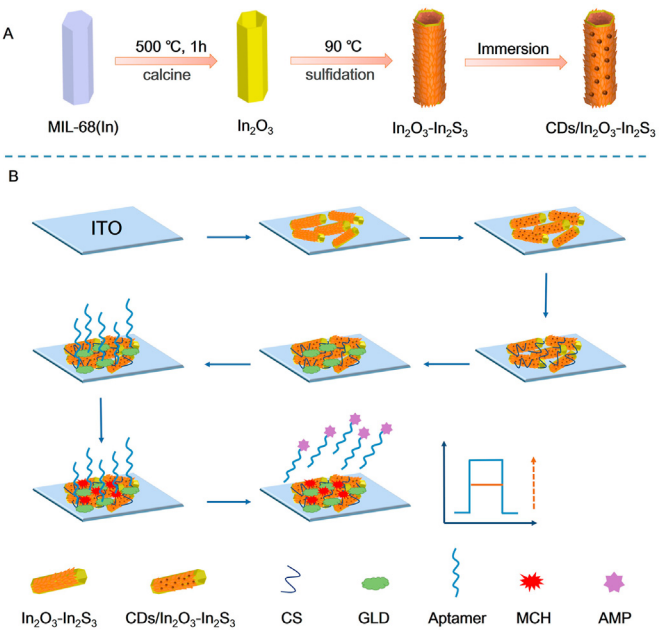


**Scheme 1.** Schematic diagram of (A) the synthetic route of $CDs/In_2O_3–In_2S_3$ composite and (B) the assembly process of PEC aptasensor for AMP detecting.

The $In_2O_3–In_2S_3$ hollow tubular heterojunction was synthesized by ion exchange method. In a typical case, 40 mg of the as-prepared $In_2O_3$ hollow tubes was scattered in 12 mL of distilled water, then 100 mg of thioacetamide was added under magnetic stirring, and the resulting mixture was transferred into a 20 mL Teflon autoclave and subjected to a hydrothermal reaction at 90 °C for a scheduled time. Then, the final products were thoroughly rinsed with absolute ethanol and distilled water, and dried in vacuum at 60 °C. The obtained products were designated as $In_2O_3–In_2S_3$-x (x = 6, 12, 18, 48 h).

### 2.2. Preparation of $CDs/In_2O_3–In_2S_3$ electrode

The CDs were prepared through a simple hydrothermal method according to the literature [38]. The detailed operation was listed in the Supporting information. To prepare the modified photoelectrode, Indium–Tin Oxides (ITO) slices (2.0 × 0.5 $cm^2$) were rinsed with ethanol, acetone, and ultrapure water for 40 min, respectively, and then dried with a stream of nitrogen.

Firstly, 9 μL of 3 mg $mL^{-1}$ $In_2O_3–In_2S_3$ suspension was cast onto the bare ITO glass. After drying, the obtained modified electrode was sintered at 180 °C for 2 h to heighten the bond strength between the film and the ITO substrate. After cooling to room temperature, a stable and compact $In_2O_3–In_2S_3$ composite modified

ITO ($In_2O_3$–$In_2S_3$/ITO) electrode was obtained. Next, the $In_2O_3$–$In_2S_3$/ITO electrode was dipped in 4 mg $mL^{-1}$ CDs solution for 9 h, and then washed carefully with ultrapure water. The desired CDs/$In_2O_3$–$In_2S_3$/ITO electrode was completed.

### 2.3. Fabrication of the PEC aptasensor

In brief, 4.5 μL chitosan (CS) solution (0.08%) was added to the resulting CDs/$In_2O_3$–$In_2S_3$/ITO electrode and dried under room temperature. Then, 4.5 μL glutaraldehyde (GLD) solution (2.5%) was dropped onto the surface of the electrode, kept at room temperature for 1 h and then thoroughly washed with deionized water to remove exceed GLD. Following, 4.5 μL of 1.5 μmol $L^{-1}$ AMP aptamer (dispersed in 0.01 mol $L^{-1}$ PBS) was grafted on the GLD/CS/CDs/$In_2O_3$–$In_2S_3$/ITO electrode and stored at 4 °C for 4 h, then rinsed with PBS (0.01 mol $L^{-1}$) to remove physically adsorbed aptamer. After drying, the aptamer/GLD/CS/CDs/$In_2O_3$–$In_2S_3$/ITO electrode was covered with 4.5 μL of 1 mmol $L^{-1}$ mercaptoethanol (MCH) solution for 40 min to block non-specific sites. And then washing with PBS (0.01 mol $L^{-1}$). The PEC aptasensor was completed and stored at 4 °C to use.

### 2.4. PEC detection of AMP

4.5 μL of AMP solution with diverse concentrations was introduced onto the MCH/aptamer/GLD/CS/CDs/$In_2O_3$–$In_2S_3$/ITO electrode separately and incubated at 4 °C for 50 min, and then the resulting AMP/MCH/aptamer/GLD/CDs/$In_2O_3$–$In_2S_3$/ITO electrodes were rinsed with PBS (0.01 mol $L^{-1}$). All the detection of AMP was performed on an electrochemical workstation (CHI 760E Chenhua Instrument Company, Shanghai, China) with a three-electrode system in PBS (pH = 7.4, 0.1 mol $L^{-1}$). During the PEC measurements, a 300 W xenon-lamp ($\lambda > 420$ nm) was used as the incident light source. The applied potential was 0 V (vs. SCE).

## 3. Results and discussion

### 3.1. Characterization of the as-prepared materials

The morphology and microstructure of the resulting samples were identified by SEM and TEM. As shown in Fig. S1, SEM images revealed that the as-prepared MIL-68(In) had a regular hexagonal rods structure with an approximate average length and width of 10 μm and 1.2 μm, respectively. After being calcined in high-temperature, the resulting $In_2O_3$ (Fig. 1A) retained a shape similar with that of the MIL-68(In) precursor, showing a hollow tubular structure with a slight surface collapse (Figs. S2A and B). However, the size of $In_2O_3$ was slightly reduced compared to MIL-68(In) and there were a mass of cracks and voids on the surface of the derivative products (Fig. 1A inset). This might be attributed to the decomposition of terephthalic acid organic ligand and the accompanying gas release, which caused shrinkage of the pristine framework and eventually formed a porous structure [39]. Fig. 1B shows the constructed $In_2O_3$–$In_2S_3$ hollow tubular heterojunction by ion exchange process with an inner diameter of about 585 nm, as we can see, the aggregated $In_2S_3$ nanosheets obtained through hydrothermal sulfurization uniformly grew on $In_2O_3$ hollow tubes, forming an intimate contact heterogeneous interface (Fig. 1D). Moreover, the TEM images further proved that the as-prepared CDs/$In_2O_3$–$In_2S_3$ displayed a distinct hollow tubular hierarchical structure characteristic (Figs. S2C and D). Beside, the TEM images of CDs were close to spherical with an average size of about 5 nm (Fig. S3). In the HRTEM images of CDs/$In_2O_3$–$In_2S_3$ (Fig. 1D-F), the formation of $In_2O_3$–$In_2S_3$ hollow tubular heterojunction was further explained, the three lattice fringes of 0.29, 0.27, 0.32 nm were correspond to (2 2 2) plane of $In_2O_3$ [40], (4 0 0) plane of $In_2S_3$ [41], and (0 0 2) plane of CDs [42], respectively, indicating the tight combination between the components of CDs/$In_2O_3$–$In_2S_3$ composite. The clearer FFT of $In_2O_3$ lattice fringe was shown in Fig. S4. Additionally, it was also confirmed that the loading of CDs was successfully achieved by the impregnation process. At the same time, the EDS spectra (Fig. 1G) and element mapping (Fig. S5) of CDs/$In_2O_3$–$In_2S_3$ composite further revealed the existence and distribution of In, O, S, and C elements.

To clarify the configuration and surface chemical state of CDs/$In_2O_3$–$In_2S_3$ composite, XPS analysis was carried out. As shown in Fig. 1H, the survey spectrum proved the elements of In, O, S and C were existed in composite, which was accordant with EDS results. The detailed analysis of XPS spectrum was demonstrated in the Supporting information.

Moreover, the phase structures of CDs, $In_2O_3$, $In_2O_3$–$In_2S_3$ and CDs/$In_2O_3$–$In_2S_3$ were characterized by XRD. As can be seen from Fig. 1I, the diffraction patterns of CDs displayed a broad peak at 23.4°, indicating the existence of an amorphous carbon atoms [43]. The diffraction patterns of MIL-68(In) derived $In_2O_3$ was consistent with the cubic $In_2O_3$ phase without findable impurities (JCPDS No. 71–2194). For $In_2O_3$–$In_2S_3$, all diffraction peaks could be recorded in cubic $In_2O_3$ and $\beta$-$In_2S_3$ (JCPDS No. 65–0459), and no additional peaks appeared, indicating the $In_2O_3$–$In_2S_3$ hollow tubular heterojunction was successfully synthesized. Moreover, with the extension of hydrothermal reaction time, the diffraction peak of $\beta$-$In_2S_3$ gradually increased, while the peak of $In_2O_3$ continuously decreased (Fig. S7). When the reaction time reached 48 h, the $In_2O_3$ was completely converted into $\beta$-$In_2S_3$. Nevertheless, no significant diffraction single of CDs was observed in the CDs/$In_2O_3$–$In_2S_3$, because of the low proportion of CDs loading. Besides, the UV–vis absorption spectrum of CDs (Fig. S8A) demonstrated two obvious characteristic peaks appeared at about 245 and 338 nm, which corresponded to the π-π* and n-π* transitions, respectively [44]. The CDs emitted blue fluorescence at about 365 nm (Fig. S8A inset), which was consistent with the reported work [33]. This result verified that CDs were successfully prepared. As shown in Fig. S8B, the as-obtained CDs emerged a distinct up-conversion PL characteristic due to a multiphoton activation process, in which the CDs could simultaneously absorb two or more photons, and cause the emission wavelength to be shorter than the excitation wavelength (anti-Stokes type emission) [45].

### 3.2. Mechanism exploration

The UV–vis diffuse-reflectance spectra (DRS) of $In_2O_3$, $In_2S_3$, $In_2O_3$–$In_2S_3$ and CDs/$In_2O_3$–$In_2S_3$ were shown in Fig. 2A. The absorption edge of $In_2O_3$ and $In_2S_3$ appeared at approximately 450 nm and 625 nm, and the band gap energy was calculated to be 2.83 eV and 2.02 eV (Fig. 2B), respectively. Compared with $In_2O_3$, the $In_2O_3$–$In_2S_3$ displayed a distinct increase of visible light absorption, owing to the in-situ growth of $In_2S_3$ nanosheets with narrow bandgap, which effectively ameliorated the light utilization of $In_2O_3$. Additionally, the absorption edge of CDs/$In_2O_3$–$In_2S_3$ exhibited a further red-shift in contrast to the $In_2O_3$–$In_2S_3$, owing to the photosensitization of CDs with up-conversion PL characteristics. This further improved the light utilization efficiency for the proposed PEC sensing platform.

The Mott-Schottky (M – S) analysis aimed to confirm the band structure of $In_2O_3$ and $In_2S_3$. As can be seen from Fig. 2C and D, the flat band potentials ($E_{fb}$) of $In_2O_3$ and $In_2S_3$ were

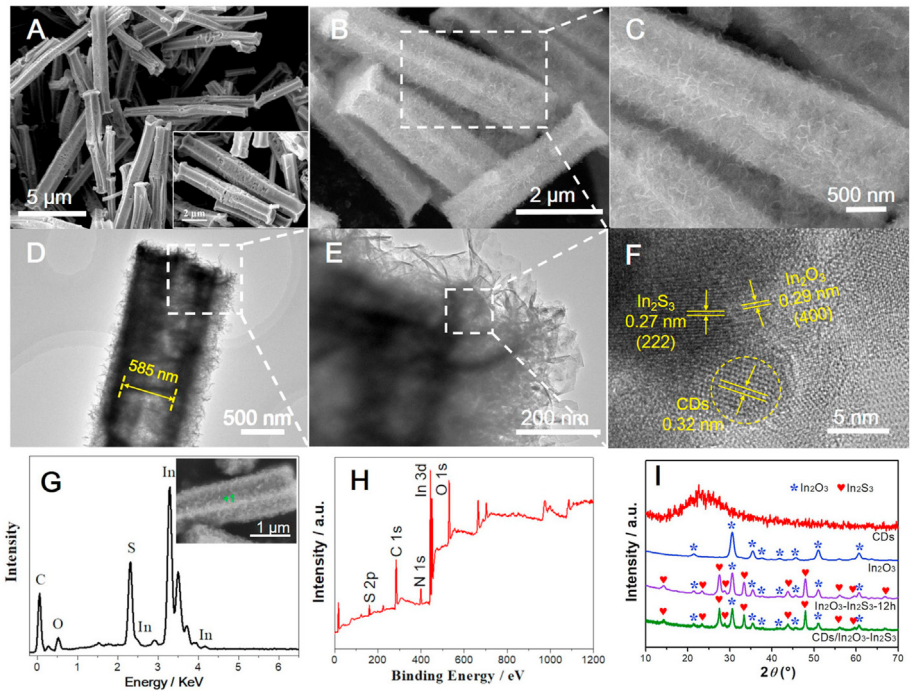


**Fig. 1.** SEM images of (A) MIL-68(In) derived $In_2O_3$ hollow tubes and (B)–(C) $In_2O_3$–$In_2S_3$ hollow tubular heterojunction; HRTEM images of (D)–(F) CDs/$In_2O_3$–$In_2S_3$; (G) EDS spectrum of CDs/$In_2O_3$–$In_2S_3$; (H) XPS spectra of CDs/$In_2O_3$–$In_2S_3$; (I) XRD patterns of CDs, $In_2O_3$, $In_2O_3$–$In_2S_3$ and CDs/$In_2O_3$–$In_2S_3$.

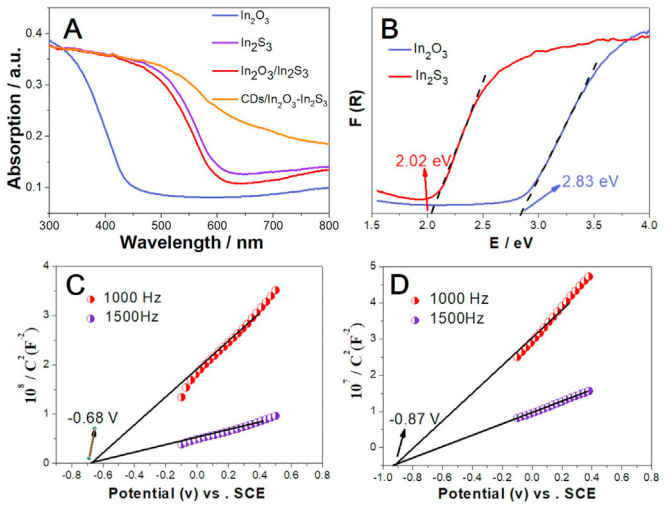


**Fig. 2.** (A) UV–vis absorption spectra and (B) band gaps of the as-synthesized samples; Mott-Schottky plot of MIL-68(In) derived (C) $In_2O_3$ and (D) $In_2S_3$.

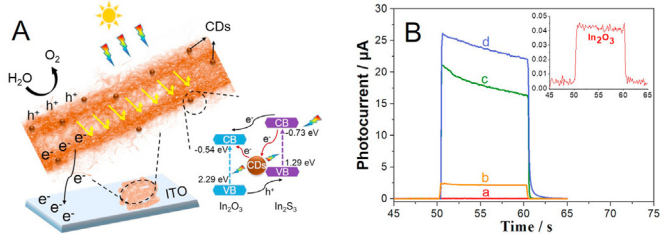


**Fig. 3.** (A) Electron-transfer mechanism of the PEC AMP-aptasensor; (B) Photocurrent responses of (a) $In_2O_3$, (b) $In_2S_3$, (c) $In_2O_3$–$In_2S_3$, and (d) CDs/$In_2O_3$–$In_2S_3$ in 0.1 mol $L^{-1}$ PBS (pH = 7.4) at 0 V bias. The inset was the photocurrent of $In_2O_3$.

approximately −0.68 V and −0.87 V (vs. SCE), equaling to a potential of −0.44 V and −0.63 V (vs. NHE). Additionally, the M − S of $In_2O_3$ and $In_2S_3$ showed a positively correlated, revealing that it had n-type behavior [46]. In general, the conduction band potentials ($E_{CB}$) of n-type semiconductor was about 0.1–0.2 V lower than $E_{fb}$ [47]. Thus, the $E_{CB}$ and valence band potentials ($E_{VB}$) of $In_2O_3$ and $In_2S_3$ were estimated to be −0.54/2.29 eV and −0.73/1.29 eV, respectively.

Photoluminescence (PL) could further verify the improvement of photoexcitation charge separation efficiency. Fig. S9 showed the PL spectra of $In_2O_3$, $In_2O_3$–$In_2S_3$ and CDs/$In_2O_3$–$In_2S_3$ composite excited at 330 nm. It is generally believed that the weaker the PL strength, the higher the separation efficiency of electron-hole pair, leading to the higher photoactivity [48]. It was obvious that the PL strength of $In_2O_3$–$In_2S_3$ was lower than that of $In_2O_3$, which was attributed to the fact that $In_2O_3$–$In_2S_3$ heterojunction effectively suppressed the recombination of photo-induced carriers. After introducing CDs, displayed the lowest PL intensity, indicating that the CDs/$In_2O_3$–$In_2S_3$ composite exhibited more efficient carrier separation efficiency.

Based on the above discussion, a reasonable charge-transfer conduction mechanism was proposed (Fig. 3A). The $In_2O_3$ and $In_2S_3$ were excited concurrently under visible light irradiation, which conformed to the II-type heterostructure and both the VB and CB of $In_2O_3$ were higher than that of $In_2S_3$. Hence, photo-induced electrons were transferred from $In_2S_3$ to $In_2O_3$, and then injected into ITO to generate photocurrent signal. The holes left in VB of $In_2O_3$ was transferred to $In_2S_3$, and then oxidized $H_2O$ to $O_2$ [46]. It is noteworthy that the hollow tubular structure of

$In_2O_3$–$In_2S_3$ heterojunction was beneficial to adjust the refractive index in the space void, thereby improve the light absorption and carrier separation efficiency. Morever, the hybrid of CDs with $In_2O_3$–$In_2S_3$ heterojunction further promote the electron-hole pairs generation and the photoelectron transmission [36]. Furthermore, the up-conversion PL effects further expand the light absorption range and light utilization efficiency [49].

The preparation process of the modified photoelectrode could be studied by recording the photocurrent response under intermittent visible-light irradiation. As illustrated in Fig. 3B, the transient photocurrent response of CDs/$In_2O_3$–$In_2S_3$ (curve d) electrode was higher than the $In_2O_3$ (curve a), $In_2S_3$ (curve b) and $In_2O_3$–$In_2S_3$ (curve c). The enhanced photocurrent was attributed to the matched band structure between $In_2S_3$ and $In_2O_3$, and the perfect conductivity and up-conversion PL properties of CDs.

### 3.3. Characterization of the aptasensor

The assembly procedure of PEC aptasensor was evaluated by EIS. As we can see from Fig. 4A, the EIS Nyquist plot consists of a semicircle in high-frequency region and a linear diagram in low-frequency region. The inset exhibited the corresponding equivalent circuit, which including the solution resistance ($R_s$), double layer capacitance ($C_{dl}$), charge transfer resistance ($R_{et}$), and Warburg impendence ($Z_\omega$). The fitted values of the equivalent circuits were simulated and calculated by *ZSimWin* software (Table S1). The unembellished ITO electrode exhibits the lowest $R_{et}$ (curve a). When the different materials CDs/$In_2O_3$–$In_2S_3$ (curve b), CS/CDs/$In_2O_3$–$In_2S_3$ (curve c), GLD/CS/CDs/$In_2O_3$–$In_2S_3$ (curve d), aptamer/GLD/CS/CDs/$In_2O_3$/$In_2S_3$ (curve e) and MCH/aptamer/GLD/CS/CDs/$In_2O_3$–$In_2S_3$ (curve f) were deposited step by step onto the ITO electrode surface, $R_{et}$ gradually increased, demonstrating that each layer of the electrode was successfully modified. Nevertheless, $R_{et}$ was significantly reduced after AMP molecule was introduced (curve g). The phenomenon should be put down to the interaction of AMP with its aptamer to form an AMP-aptamer complex, and then the formed AMP-aptamer complex fell off the sensing interface.

Photocurrent response of different fabricated process for PEC aptasensing platform was investigated (Fig. 4B). Compared to unmodified ITO electrodes (curve a), the photocurrent intensity of CDs/$In_2O_3$–$In_2S_3$/ITO was significantly enhanced and reached the maximum (curve b). Then CS, GLD, aptamer, and MCH were sequentially deposited on the CDs/$In_2O_3$–$In_2S_3$/ITO electrode, gradually decreased photocurrent was observed, suggesting that their insulation and spatial steric effect increased resistance of the modified electrode. However, after the AMP molecule specifically bound to the aptamer, the aptamer was released from the electrode surface and the photocurrent increased (curve g). The above results testified that the PEC aptasensor had been successfully developed.

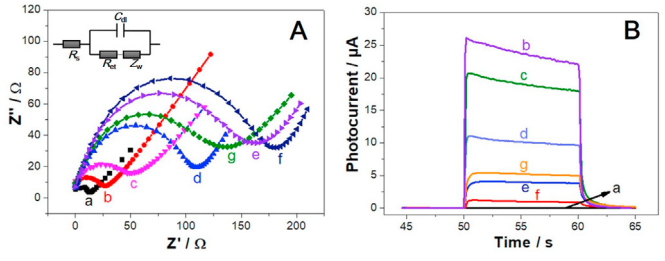


**Fig. 4.** (A) EIS and (B) photocurrent responses of different modified electrode: (a) ITO, (b) CDs/$In_2O_3$–$In_2S_3$/ITO, (c) CS/CDs/$In_2O_3$–$In_2S_3$/ITO, (d) GLD/CS/CDs/$In_2O_3$–$In_2S_3$/ITO, (e) aptamer/GLD/CS/CDs/$In_2O_3$–$In_2S_3$/ITO, (f) MCH/aptamer/GLD/CS/CDs/$In_2O_3In_2S_3$/ITO and (g) 100 ng $mL^{-1}$ AMP/MCH/aptamer/GLD/CS/CDs/$In_2O_3$–$In_2S_3$/ITO. The EIS spectra were measured in 2.5 mol $L^{-1}$ $[Fe(CN)_6]^{3-/4-}$ containing 0.1 mol $L^{-1}$ KCl. The PEC experiment was operated in 0.1 mol $L^{-1}$ PBS (pH = 7.4) at 0 V bias.

### 3.4. Optimization of conditions

In order to investigate the property of the constructed PEC aptasensor, various relevant experimental conditions were optimized. Fig. S10A exhibited the photocurrent of $In_2O_3$–$In_2S_3$-x modified ITO electrode. It could be seen that $In_2O_3$–$In_2S_3$-12 exhibited optimal photoelectric performance. Herein, the $In_2O_3$–$In_2S_3$-12 was adopted for the fabricating of PEC sensing platform.

Fig. S10B showed the photocurrent intensities of CDs/$In_2O_3$–$In_2S_3$/ITO electrodes in disparate soaking period in 4 mg $mL^{-1}$ CDs solution. The photocurrent of CDs/$In_2O_3$–$In_2S_3$/ITO electrode increased as the immersion time increased from 2 h to 9 h, due to the appropriate CDs could effectively utilize visible light to accelerate the transmission of electrons. However, prolonged immersion resulted in reduced photocurrent, because the excessive CDs would concentrate on the surface of $In_2O_3$–$In_2S_3$, inhibited electron transfer and hindered light absorption of $In_2O_3$–$In_2S_3$ [50]. Therefore, the CDs/$In_2O_3$–$In_2S_3$/ITO electrode was soaked for 9 h to obtain the optimal photocurrent response.

As a key factor affecting the performance of PEC aptasensor, the effect of pH was investigated. It can be seen from Fig. S10C, the maximum photocurrent was reached at a pH of 7.4, owing to the biological activity of the protein could be preserved in a neutral environment. Hence, pH 7.4 was chosen for maintaining the best AMP aptamer activity.

The concentration of the adopted aptamer also affect the performance of the proposed aptasensor. As showed in Fig. S10D, the transient photocurrent response gradually decreased as the AMP aptamer concentration increased from 0 to 2 μmol $L^{-1}$. Nevertheless, when the AMP aptamer concentration exceeded 1.5 μmol $L^{-1}$, the captured photocurrent signal tends to be stable and hardly decreased. So, 1.5 μmol $L^{-1}$ was chosen as the optimal concentration for the subsequent experiment.

### 3.5. PEC detects of AMP

Under the optimal conditions, the aptasensor was constructed to achieve quantitative detection of different concentrations of AMP. As can be seen from Fig. 5A, the photocurrent was reposeful and positively correlated with AMP concentration under intermittent visible light irradiation. Fig. 5B displayed the photocurrent response linearly enhanced with increasing AMP concentration from 0.001 ng $mL^{-1}$ to 300 ng $mL^{-1}$. The liner regression equation was $I = 0.855\ \lg c + 3.6$, with the correction coefficient ($R^2$) of 0.996, and the LOD of the PEC AMP-aptasensor was 0.6 pg $mL^{-1}$ (S/N = 3). Compared to other existing AMP detection methods (Table S2), the as-prepared PEC AMP-aptasensor presented acceptable response range and satisfactory detection limit.

### 3.6. Selectivity, stability and reproducibility

In order to assess the selectivity of the prepared aptasensor, several typical antibiotics including tetracycline (TC), chloramphenicol (CAP), amoxicillin (AMO) were investigated for the interference of the proposed aptasensor photocurrent signal. Fig. 5C revealed the photocurrent response to a concentration of 100 ng $mL^{-1}$ for each substance, indicating that the photocurrent intensity of AMP was significantly higher than other interferences and had acceptable selectivity. Besides, adding mixture of AMP had no obvious effects in photocurrent compared to pure AMP, which meant that the presence

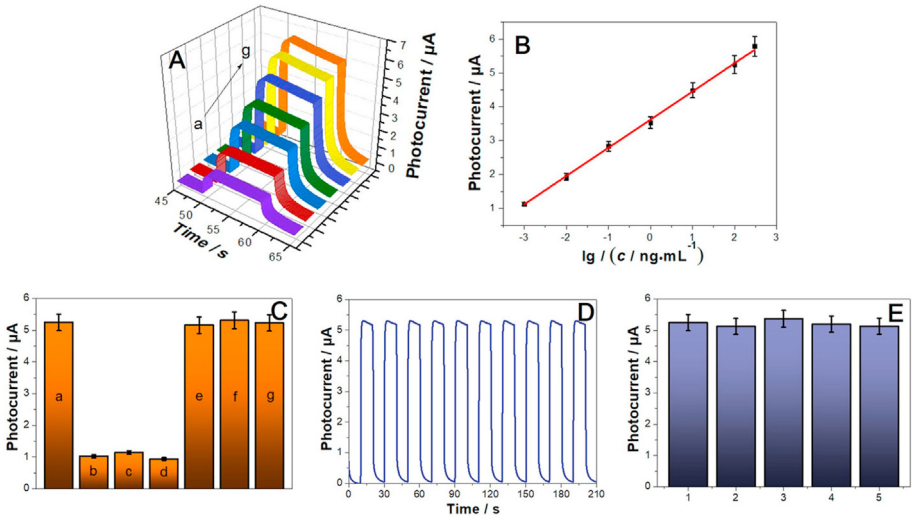


**Fig. 5.** (A) Photocurrent responses under visible light of the AMP aptasensor to (a–g) 0.001, 0.01, 0.1, 1, 10, 100, 300 ng mL$^{-1}$ AMP; (B) Logarithmic calibration curve of different AMP concentrations; (C) Selectivity of the as-prepared aptasensor to AMP, (a) AMP, (b) chloramphenicol, (c) tetracycline, (d) amoxicillin, (e) AMP + chloramphenicol, (f) AMP + tetracycline, (g) AMP + amoxicillin; (D) Stability of the PEC aptasensor with 100 ng mL$^{-1}$ AMP; (E) The reproducibility of the proposed PEC aptasensor. All the tests were performed in 0.1 mol L$^{-1}$ PBS (pH = 7.4) at 0 V bias. Error bars show the standard deviation of repeated measurements (n = 3).

of other antibiotics did not evidently interfere with the detection of AMP. The results testified that the designed aptasensor had excellent selectivity and satisfactory anti-interference ability.

Fig. 5D illustrated the stability of the proposed aptasensing platform. There was no remarkable change in the intensity of the photocurrent signal during 10 on/off irradiation cycles, and the PEC output signals was stable, indicating the excellent stability of the PEC aptasensing platform. Furthermore, the storage stability of the developed aptasensor was inspected (Fig. S11). After the proposed AMP-aptasensor stored at 4 °Cfor half a month and one month, the photocurrent response was maintained at 95% and 92% of the initial photocurrent, respectively, suggesting that it had great storage stability.

To evaluate the reproducibility of the PEC aptasensor (Fig. 5E), 5 independent electrodes modified with 100 ng mL$^{-1}$ AMP were tested under the same experimental conditions. The relative standard deviation (RSD) was 1.9%, indicating the outstanding reproducibility of the proposed PEC aptasensor.

### 3.7. Real sample analysis

The designed PEC aptasensor was applied to the detection of AMP in lake water samples through standard addition method. And the test results were verified by HPLC as a reference method. As displayed in Table S3, the determined results of different concentrations of AMP samples added to the lake water were in good agreement by two methods. The recovery range of AMP was 98.4%–103.1%, and the RSD was from 1.3% to 3.6%. These results indicated that the proposed PEC AMP-aptasensor could be used in the accurate detection of AMP in environmental water samples.

## 4. Conclusions

In summary, a novel CDs/$In_2O_3$–$In_2S_3$ composite with excellent photoactivity was first synthesized and employed to fabricate self-powered PEC aptasensor for AMP detecting. The $In_2O_3$–$In_2S_3$ hollow tubular heterojunction, which constructed by the in-situ growth of $In_2S_3$ nanosheets on the surfaces of $In_2O_3$ hollow tubes, significantly promoted the transfer and separation of photogenerated carriers, and provided a larger specific surface area and rich active sites for the PEC aptasensing platform. Furthermore, the hybridization of CDs with $In_2O_3$–$In_2S_3$ hollow tubular heterojunction further enhanced the visible light utilization and promoted the photoelectron transfer of photoelectrode, thus remarkably improved the PEC sensing performance. Based on the change of photocurrent intensity at zero-bias caused by the specific binding of aptamer and AMP, the high selectivity and sensitive quantitative detection of AMP could be realized with the detection limit of 0.6 pg mL$^{-1}$. Furthermore, the proposed self-powered PEC aptasensing platform showed potential application prospect in actual environmental samples monitoring.

## Declaration of competing interest

The authors declare that they have no known competing financial interests or personal relationships that could have appeared to influence the work reported in this paper.

## Acknowledgments

This study was supported by the National Key Scientific Instrument and Equipment Development Project of China (No. 21627809), National Natural Science Foundation of China (Nos. 21505051, 21575050, 21607055, 21777056), the Youth Creative Talents Introduction and Cultivation Plan in Universities of Shandong Province, Jinan Scientific Research Leader Workshop Project (2018GXRC024). Ju thanks the Special Foundation for Taishan Scholar Professorship of Shandong Province (No. ts201712052) and UJN.

## Appendix A. Supplementary data

Supplementary data to this article can be found online at https://doi.org/10.1016/j.jmat.2021.01.002.

## References

[1] Drawz SM, Bonomo RA. Three decades of beta-lactamase inhibitors. Clin Microbiol Rev 2010;23(1):160–201.
[2] Wang T, Yin H, Zhang Y, Wang L, Du Y, Zhuge Y, et al. Electrochemical aptasensor for ampicillin detection based on the protective effect of aptamer-

antibiotic conjugate towards dpnii and exo iii digestion. Talanta 2019;197:42–8.
[3] Song KM, Jeong E, Jeon W, Cho M, Ban C. Aptasensor for ampicillin using gold nanoparticle based dual fluorescence-colorimetric methods. Anal Bioanal Chem 2012;402(6):2153–61.
[4] Ibrahim FA, Nasr JJM. Direct determination of ampicillin and amoxicillin residues in food samples after aqueous sds extraction by micellar liquid chromatography with uv detection. Anal Methods 2014;6(5):1523–9.
[5] Andreou C, Mirsafavi R, Moskovits M, Meinhart CD. Detection of low concentrations of ampicillin in milk. Analyst 2015;140(15):5003–5.
[6] Luo Z, Wang Y, Lu X, Chen J, Wei F, Huang Z, et al. Fluorescent aptasensor for antibiotic detection using magnetic bead composites coated with gold nanoparticles and a nicking enzyme. Anal Chim Acta 2017;984:177–84.
[7] Yang Z, Ding X, Guo Q, Wang Y, Lu Z, Ou H, et al. Second generation of signaling-probe displacement electrochemical aptasensor for detection of picomolar ampicillin and sulfadimethoxine. Sensor Actuator B Chem 2017;253:1129–36.
[8] Zhang K, Wang ZL, Yang Y. Enhanced P3HT/ZnO nanowire array solar cells by pyro-phototronic effect. ACS Nano 2016;10(11):10331–8.
[9] Kim WS, Moon YK, Lee S, Kang BW, Kwon TS, Kim KT, et al. Copper source/drain electrode contact resistance effects in amorphous indium–gallium–zinc-oxide thin film transistors. Phys Status Solidi-R 2010;3(7–8):239–41.
[10] Yang Y, Qi J, Liao Q, Li H, Wang Y, Tang L, et al. High-performance piezoelectric gate diode of a single polar-surface dominated ZnO nanobelt 2009;20(12):125201.
[11] Du X, Jiang D, Li H, Hao N, You T, Wang K. An intriguing signal-off responsive photoelectrochemical aptasensor for ultrasensitive detection of microcystin-lr and its mechanism study. Sensor Actuator B Chem 2018;259:316–24.
[12] Shu J, Tang D. Current advances in quantum-dots-based photoelectrochemical immunoassays. Chem Asian J 2017;12(21):2780–9.
[13] Zhao K, Ouyang B, Bowen CR, Wang Z, Yang Y. One-structure-based multi-effects coupled nanogenerators for flexible and self-powered multi-functional coupled sensor systems. Nanomater Energy, 2020, 71(104632).
[14] Ouyang B, Zhang K, Yang Y. Photocurrent polarity controlled by light wavelength in self-powered ZnO nanowires/SnS photodetector system. iScience 2018;1(16–23).
[15] Ouyang B, Chang C, Zhao L, Wang Z, Yang Y. Thermo-photoelectric coupled effect induced electricity in N-type SnSe:Br single crystals for enhanced self-powered photodetectors. Nanomater Energy 2019;66(104111).
[16] Kang Z, Yan X, Wang Y, Zhao Y, Bai Z, Liu Y, et al. Self-powered photoelectrochemical biosensing platform based on Au NPs@ZnO nanorods array. Nano Res 2016;9(2):344–52.
[17] Feng Y, Yan T, Wu T, Zhang N, Yang Q, Sun M, et al. A label-free photoelectrochemical aptasensing platform base on plasmon au coupling with mof-derived $In_2O_3$@g-$C_3N_4$ nanoarchitectures for tetracycline detection. Sensor Actuator B Chem 2019;298.
[18] Liu C, Huang C, Chang H. Highly selective DNA-based sensor for lead(ii) and mercury(ii) ions. Anal Chem 2009;81(6):2383–7.
[19] Hasanzadeh M, Razmi N, Mokhtarzadeh A, Shadjou N, Mahboob S. Aptamer based assay of plated-derived grow factor in unprocessed human plasma sample and MCF-7 breast cancer cell lysates using gold nanoparticle supported alpha-cyclodextrin. Int J Biol Macromol 2018;108:69–80.
[20] Jolly P, Tamboli V, Harniman RL, Estrela P, Allender CJ, Bowen JL. Aptamer-mip hybrid receptor for highly sensitive electrochemical detection of prostate specific antigen. Biosens Bioelectron 2016;75:188–95.
[21] Wang N, Luo X, Han L, Zhang Z, Zhang R, Olin H, et al. Structure, performance, and application of $BiFeO_3$ nanomaterials. Nano-Micro Lett 2020;12(1):218–40.
[22] Yang Y, Guo W, Qi J, Zhang Y. Flexible piezoresistive strain sensor based on single Sb-doped ZnO nanobelts. Appl Phys Lett 2010;97(223107).
[23] Yang Y, Qi J, Liao Q, Zhang Y, Tang L, Qi Z. Synthesis and characterization of Sb-doped ZnO nanobelts with single-side zigzag boundaries. J Phys Chem C 2008;112(46):17916–9.
[24] Jiang Y, Wang Y, Wu H, Wang Y, Zhang R, Olin H. Laser-etched stretchable graphene–polymer composite array for sensitive strain and viscosity sensors. Nano-Micro Lett 2019;11(1):2311–6706.
[25] Fan L, Liu P, Yan X, Gu L, Yang Z, Yang H, et al. Atomically isolated nickel species anchored on graphitized carbon for efficient hydrogen evolution electrocatalysis. Nat Commun 2016;7:7.
[26] Zhang L, Wu H, Madhavi S, Hng HH, Lou X. Formation of $Fe_2O_3$ microboxes with hierarchical shell structures from metal-organic frameworks and their lithium storage properties. J Am Chem Soc 2012;134(42):17388–91.
[27] Sun J, Zhang J, Zhang M, Antonietti M, Fu X, Wang X. Bioinspired hollow semiconductor nanospheres as photosynthetic nanoparticles. Nat Commun 2012;3.
[28] Zheng D, Cao X, Wang X. Precise formation of a hollow carbon nitride structure with a janus surface to promote water splitting by photoredox catalysis. Angew Chem Int Ed 2016;55(38):11512–6.
[29] Wang S, Guan B, Lu Y, Lou X. Formation of hierarchical $In_2S_3$-$CdIn_2S_4$ heterostructured nanotubes for efficient and stable visible light $CO_2$ reduction. J Am Chem Soc 2017;139(48):17305–8.
[30] Wang S, Guan B, Lou X. Construction of $ZnIn_2S_4$-$In_2O_3$ hierarchical tubular heterostructures for efficient $CO_2$ photoreduction. J Am Chem Soc 2018;140(15):5037–40.
[31] Ren J, Yuan K, Wu K, Zhou L, Zhang Y. A robust CdS/$In_2O_3$ hierarchical heterostructure derived from a metal-organic framework for efficient visible-light photocatalytic hydrogen production. Inorg Chem Front 2019;6(2):366–75.
[32] Fei W, Song Y, Li N, Chen D, Xu Q, Li H, et al. Hollow $In_2O_3$@$ZnFe_2O_4$ heterojunctions for highly efficient photocatalytic degradation of tetracycline under visible light. Environ Sci-Nano 2019;6(10):3123–32.
[33] Xu X, Yan B. Fabrication and application of a ratiometric and colorimetric fluorescent probe for $Hg^{2+}$ based on dual-emissive metal-organic framework hybrids with carbon dots and $Eu^{3+}$. J Mater Chem C 2016;4(7):1543–9.
[34] Zhang P, Song T, Wang T, Zeng H. In-situ synthesis of cu nanoparticles hybridized with carbon quantum dots as a broad spectrum photocatalyst for improvement of photocatalytic H-2 evolution. Appl Catal B Environ 2017;206:328–35.
[35] Guo M, Wang S, Zhao L, Guo Z. High-performance asymmetric supercapacitor based on flowery nickel-zinc phosphate microspheres with carbon dots. Electrochim Acta 2018;292:299–308.
[36] Cheng W, Pan J, Yang J, Zheng Z, Lu F, Chen Y. A photoelectrochemical aptasensor for thrombin based on the use of carbon quantum dot-sensitized $TiO_2$ and visible-light photoelectrochemical activity. Microchim Acta 2018;185(5).
[37] Jin L, Liu Q, Sun W. Size-controlled indium(iii)-benzenedicarboxylate hexagonal rods and their transformation to $In_2O_3$ hollow structures. CrystEngComm 2013;15(23):4779–84.
[38] Zhu S, Meng Q, Wang L, Zhang J, Song Y, Jin H, et al. Highly photoluminescent carbon dots for multicolor patterning, sensors, and bioimaging. Angew Chem Int Ed 2013;52(14):3953–7.
[39] Shi S, Zhang F, Lin H, Wang Q, Shi E. Enhanced triethylamine-sensing properties of p-n heterojunction $Co_3O_4$/$In_2O_3$ hollow microtubes derived from metal–organic frameworks. Sensor Actuator B Chem 2018;262:739–49.
[40] Xu R, Li H, Zhang W, Yang Z, Liu G, Xu Z, et al. The fabrication of $In_2O_3$/$In_2S_3$/Ag nanocubes for efficient photoelectrochemical water splitting. Phys Chem Chem Phys 2016;18(4):2710–7.
[41] Zhang F, Li X, Zhao Q, Zhang Q, Tade M, Liu S. Facile and controllable modification of 3D $In_2O_3$ microflowers with $In_2S_3$ nanoflakes for efficient photocatalytic degradation of gaseous ortho-dichlorobenzene. J Phys Chem C 2016;120(34):19113–23.
[42] Khan UA, Liu J, Pan J, Ma H, Zuo S, Yu Y, et al. Fabrication of highly efficient and hierarchical CdS QDs/CQDs/H-$TiO_2$ ternary heterojunction: surpassable photocatalysis under sun-like illumination. Ind Eng Chem Res 2019;58(1):79–91.
[43] Liu Y, Xiao N, Gong N, Wang H, Shi X, Gu W, et al. One-step microwave-assisted polyol synthesis of green luminescent carbon dots as optical nanoprobes. Carbon 2014;68:258–64.
[44] He C, Peng L, Lv L, Cao Y, Tu J, Huang W, et al. In situ growth of carbon dots on $TiO_2$ nanotube arrays for pec enzyme biosensors with visible light response. RSC Adv 2019;9(26):15084–91.
[45] Zhuo S, Shao M, Lee S-T. Upconversion and downconversion fluorescent graphene quantum dots: ultrasonic preparation and photocatalysis. ACS Nano 2012;6(2):1059–64.
[46] Xu H, Wang Y, Dong X, Zheng N, Ma H, Zhang X. Fabrication of $In_2O_3$/$In_2S_3$ microsphere heterostructures for efficient and stable photocatalytic nitrogen fixation. Appl Catal B Environ 2019;257:117932.
[47] Li W, Li D, Zhang W, Hu Y, He Y, Fu X. Microwave synthesis of $Zn_xCd_{1-x}S$ nanorods and their photocatalytic activity under visible light. J Phys Chem C 2010;114(5):2154–9.
[48] Li Y, Luo S, Wei Z, Meng D, Ding M, Liu C. Electrodeposition technique-dependent photoelectrochemical and photocatalytic properties of an $In_2S_3$/$TiO_2$ nanotube array. Phys Chem Chem Phys 2014;16(9):4361–8.
[49] Huang X, Yang L, Hao S, Zheng B, Yan L, Qu F, et al. N-doped carbon dots: a metal-free co-catalyst on hematite nanorod arrays toward efficient photoelectrochemical water oxidation. Inorg Chem Front 2017;4(3):537–40.
[50] Cheng W, Zheng Z, Yang J, Chen M, Yao Q, Chen Y, et al. The visible light-driven and self-powered photoelectrochemical biosensor for organophosphate pesticides detection based on nitrogen doped carbon quantum dots for the signal amplification. Electrochim Acta 2019;296:627–36.

**Tao Yan** received the Ph.D. degree from Beijing Institute of Technology (BIT), Beijing, China. He is an associate professor of school of resource and environment at University of Jinan, Shandong, China. His research interests focus on the construction of photoelectric functional materials for biosensor, energy and environment applications.